

# Three-dimensional visible light capsule enclosing perfect super-sized darkness via anti-resolution

Chao Wan<sup>1\*</sup>, Kun Huang<sup>1\*</sup>, Tiancheng Han<sup>1\*</sup>, Eunice S. P. Leong<sup>2</sup>, Weiqiang Ding<sup>1</sup>, Lei Zhang<sup>1</sup>, Tat-Soon Yeo<sup>1</sup>, Xia Yu<sup>3</sup>, Jinghua Teng<sup>2</sup>, Dang Yuan Lei<sup>4</sup>, Stefan A. Maier<sup>5</sup>, Boris Luk'yanchuk<sup>6</sup>, Shuang Zhang<sup>7</sup> and Cheng-Wei Qiu<sup>1†</sup>

<sup>1</sup>Department of Electrical and Computer Engineering, National University of Singapore, 4 Engineering Drive 3, Singapore 117576, Singapore

<sup>†</sup>Email: [eleqc@nus.edu.sg](mailto:eleqc@nus.edu.sg); Tel: (65) 65162559; Fax: (65) 67791103

\*These authors contribute equally to this work.

<sup>2</sup>Institute of Materials Research and Engineering, Agency for Science, Technology and Research, 3 Research Link, Singapore 117602, Singapore

<sup>3</sup>Singapore Institute of Manufacturing Technology, Agency for Science, Technology and Research, 71 Nanyang Drive, Singapore 638075, Singapore

<sup>4</sup>Department of Applied Physics, The Hong Kong Polytechnic University, Kowloon, Hong Kong

<sup>5</sup>The Blackett Laboratory, Department of Physics, Imperial College London, London SW7 2AZ, UK

<sup>6</sup>Data Storage Institute, Agency for Science, Technology and Research, 5 Engineering Drive 1, Singapore 117608, Singapore

<sup>7</sup>School of Physics & Astronomy, University of Birmingham, Birmingham, B15 2TT, UK

## 1. Fabrication of the binary phase mask

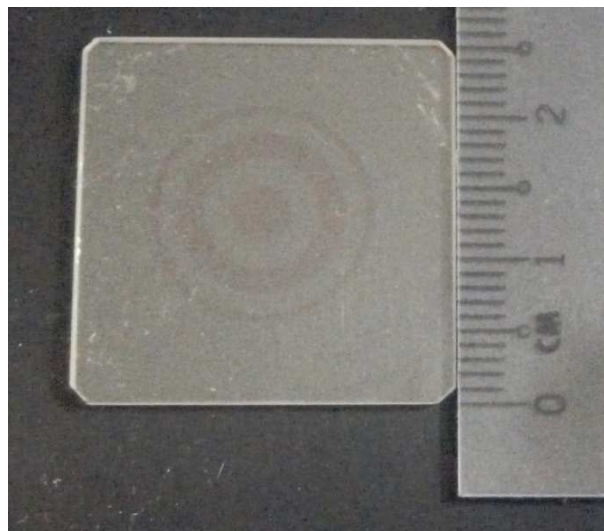


Figure S1. Photograph of the fabricated binary mask. The geometry of the binary phase mask:  $r_1=1.975\text{mm}$ ,  $r_2=3.85\text{mm}$ ,  $r_3=5.55\text{mm}$ ,  $r_4=6.925\text{mm}$  and  $r_5=7.5\text{mm}$ . The diameter of the efficient phase region in this mask is 15mm.

A 25.4×25.4×1mm quartz substrate is first cleaned with acetone and Isopropyl Alcohol (IPA) in an ultrasonic bath. AZ5214 resist is then spin coated on the substrate and pre-baked at 90°C for 30 minutes to remove the solvent. The sample was exposed under UV light in a bond aligner (SUSS MicroTec, MA8/BA6) with a photomask. The exposed regions were removed in AZ developer. After developing, the sample was post-baked at 120°C for 30 minutes. MgF<sub>2</sub> was evaporated onto the patterned sample using an e-beam evaporator (Denton Vacuum, Explorer). The base pressure was 1.1e-6 Torr and the thickness of the film was 826 nm. After evaporation, lift-off process was carried out in acetone to form the binary phase lens. The photograph of fabricated binary mask is shown in Fig. S1.

## 2. Reference experiment with spatial light modulator

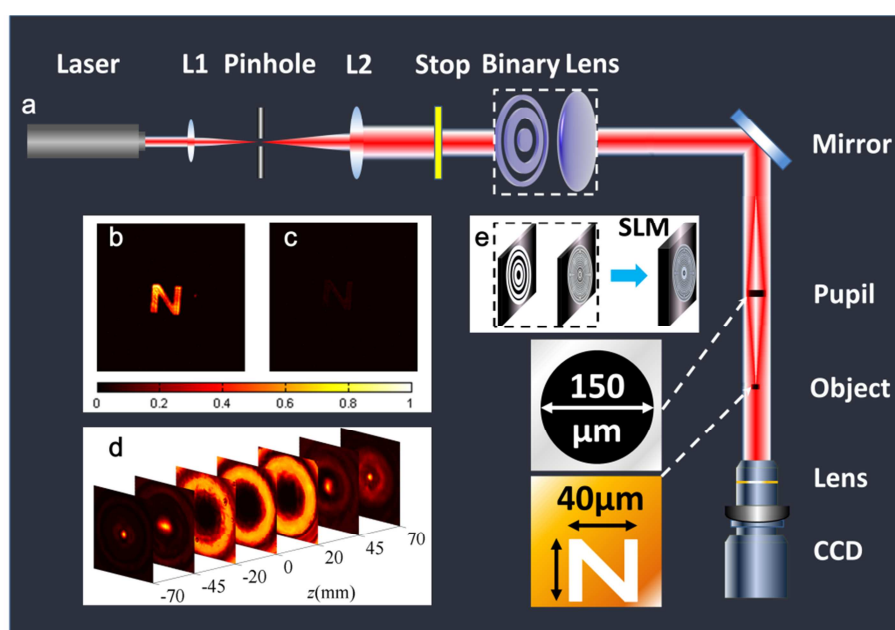


Figure S2. Reference experiment when the binary mask is replaced with a spatial light modulator. (a) Schematic of the experiment. (b) When the mask phase and the lens phase are simultaneously adopted by the SLM, light can bypass the opaque pupil and illuminate the object beneath. (c) When either mask or lens phase is adopted separately, the light is blocked by the opaque circular area. Almost no light passes the pupil and a very dark "N" is captured by CCD. (d) Measured intensity on 7 transversal planes, on both sides of the central plane ( $z=0$ ). (e) The total phase profile of binary and lens is mimicked with SLM.

### 3. Experimental Section

The experiment is carried out on an optical table of 3 m long. A linearly polarized incident laser is expanded by a beam expander comprised of two lenses and one 10  $\mu\text{m}$ -diameter pinhole. After going through a stop, the light illuminates the binary phase mask and a focusing lens (or equivalent SLM). A mirror is used to change the optical path considering the limitation of table length. An object (letter 'N') is located behind the pupil. The distance between the pupil and object is 20 mm. A CCD camera (IDS UI-2240) with a 20 $\times$  camera lens is used to record the intensity.

In the experiment using binary phase mask fabricated on the quartz substrate, the wavelength of incident light is 632.8nm and the focusing lens has the NA of 0.0075 with its focal length of 1m and the size of 15mm in diameter, which is the same with the stop size and the maximum diameter of binary phase mask. The phase delay  $\pi$  between two neighboring belts in the mask is realized by their height difference of 692nm since the refraction index of quartz is 1.4507 at 632.8nm.

In the experiment using SLM, the phase modulation mask is created by a phase-type HOLOEYE LC2002 with a pixel pitch of 32  $\mu\text{m}$  at the wavelength 532nm. A small gap with size of about 8  $\mu\text{m}$  exists between two neighboring pixels. When the light passing through the gap is focused by a lens, a spot will be generated at the focal plane of focusing lens regardless of the phase of SLM. Since a low numerical-aperture (NA) lens is equivalent to a lens phase of  $\exp[-i\pi r^2/(f\lambda)]$  in Fourier optics with  $f$  being the focal length, the presence of the NA in Fig. 2a is thus replaced by a lens-phase to be equivalently realized by the SLM. The SLM produces the mask phase and the lens phase with  $f = 2\text{m}$  simultaneously. The stop has the size of 19.2mm so that the lens realized by SLM has the NA of 0.0048.

### 4. Design of binary phase plate for realizing the anti-resolution PSF

In the main text, Eqs (2-4) demonstrates the tight focusing of the vector beams (i.e. radially and azimuthally polarized beams) by using a high NA lens. In tightly focusing of vector beams, the electric field in the focal region has the strong dependence on the polarization of incident vector beams, e.g. Eqs. (2-3) for radially polarized beam and Eq. (4) for azimuthally polarized beam [S1]. It is not convenient to describe the design of binary phase in a general way. For the sake of simplicity, we take the

focusing lens with low NA for example. In this case, the polarization effect in the focal region is not significant and can be neglected so that, for the incident beams with all the polarizations, the electric field in the focal region can be described in a unified way by using a scalar focusing of light with a low NA lens. For the scalar focusing of a low NA circular lens with focal length  $f$ , the optical field in the focal region can be expressed by [S2]

$$U(\rho, z) = \frac{i2\pi}{\lambda z} e^{ik(z + \frac{\rho^2}{2z})} \int_0^R u_0(r) \cdot e^{\frac{ikr^2}{2z}} e^{-\frac{ikr^2}{2f}} J_0\left(\frac{kr\rho}{z}\right) r dr, \quad (\text{S1})$$

where  $R$  is the radius of the focusing lens,  $u_0(r)$  is the electric field incident on the focusing lens, the exponential item  $\exp(-ikr^2/f)$  is the equivalent phase factor of the low NA lens which is located at  $z=0$ , which implies that the electric field at the focal plane is obtained by setting  $z=f$  in Eq. (S1). According to the concept of anti-resolution proposed in the main text, we should manipulate its PSF to realize the anti-resolution at the focal plane so that the electric field at the focal plane should be paid much attention. In Eq. (S1) by setting  $z=f$  and omitting its constant factor  $i2\pi/(\lambda f) \cdot \exp[ik(z+0.5\rho^2/f)]$ , we have the electric field at the focal plane

$$\begin{aligned} U(\rho) &= \int_0^R u_0(r) J_0\left(\frac{kr\rho}{f}\right) r dr = \sum_{n=1}^N \int_{r_{n-1}}^{r_n} (-1)^n J_0\left(\frac{kr\rho}{f}\right) r dr \\ &= \sum_{n=1}^N (-1)^n \left(\frac{f}{k\rho}\right)^2 [t J_1(t)]_{k\rho r_{n-1}/f}^{k\rho r_n/f}, \quad t = k\rho r/f \\ &= \sum_{n=1}^N (-1)^n \left[ r_n^2 \frac{J_1(k\rho r_n/f)}{k\rho r_n/f} - r_{n-1}^2 \frac{J_1(k\rho r_{n-1}/f)}{k\rho r_{n-1}/f} \right], \quad (\text{S2}) \\ &= f^2 \sum_{n=1}^N (-1)^n \left[ \sin^2 \theta_n \frac{J_1(k\rho \sin \theta_n)}{k\rho \sin \theta_n} - \sin^2 \theta_{n-1} \frac{J_1(k\rho \sin \theta_{n-1})}{k\rho \sin \theta_{n-1}} \right], \quad \sin \theta_n = r_n/f \\ &= f^2 \left[ (-1)^N \sin^2 \theta_N \frac{J_1(k\rho \sin \theta_N)}{k\rho \sin \theta_N} + 2 \sum_{n=1}^{N-1} (-1)^n \sin^2 \theta_n \frac{J_1(k\rho \sin \theta_n)}{k\rho \sin \theta_n} \right] \end{aligned}$$

where the incident beam is uniform and modulated by a  $N$ -belt binary phase so that  $u_0(r) = \exp(i\varphi(r))$ ,  $\sin \theta_n = r_n/f$  for the focusing lens obeys the sine condition,  $\theta_n$  is the focusing angle, with  $\theta_0=0$  and the maximum angle  $\theta_N = \sin^{-1}(\text{NA})$ , as shown by Eq. 5 in the main text. Interestingly, we find that Eq. (S2) provides an analytical model, without any integral involved, to approximate the electric field at the focal plane. By using Eq. (S2), we can obtain the arbitrary intensity pattern when changing the unknown parameter  $\theta_n$  ( $n=1, 2, \dots, N-1$ ).

Before we introduce the method to obtain the anti-resolution at the focal plane, the

physical concept of anti-resolution should be revisited on basis of the Eq. (S2). In anti-resolution, its PSF as shown in Fig. 1d has the zero intensity at  $\rho=0$  (suppressing the mainlobe intensity), the approaching zero intensity in the range  $0<\rho<D/2$  (widening the mainlobe) and the largest sidelobe intensity (enhancing the sidelobe). In order to realize the goal of suppressing the mainlobe intensity in anti-resolution, we just set the intensity to be zero at  $\rho=0$ , leading to the equation

$$(-1)^N \sin^2 \theta_N + 2 \sum_{n=1}^{N-1} (-1)^n \sin^2 \theta_n = 0. \quad (\text{S3})$$

In Eq. (S3), the  $N-1$  unknown parameters  $\theta_n$  ( $n=1, 2, \dots, N-1$ ) indicate the infinite solutions to realize the goal of suppressing the mainlobe, which implies that it is possible to fix one solution if more constraints is imposed to Eq. (S3), e.g. reserving  $N-2$  zero-intensity locations in the region  $0<\rho<D/2$  so as to widen the mainlobe (the second goal in anti-resolution). For the third goal of enhancing the sidelobe, we do not need to make any measure to realize it because the high sidelobe is the natural result in the viewpoint of energy conservation for the approaching-zero intensity in the range  $0\leq\rho<D/2$ . Therefore, it is physically feasible to construct a PSF with anti-resolution. In fact, the zero intensity in the region  $0\leq\rho<D/2$  shown in Fig. (S3) is mainly attributed to the local destructive interference caused by the  $0-\pi$  phase modulation of binary element.

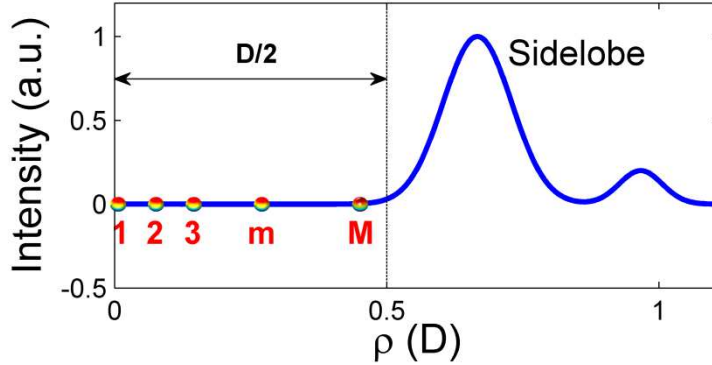


Fig. S3 The radial (along  $\rho$ ) pattern of the anti-resolution PSF. The prescribed positions from 1 to  $\mathbf{M}$  ( $\mathbf{M}=\mathbf{N}-1$ ) in the range  $0\leq\rho<D/2$  are shown by the color spots and located at the zero-intensity part of the intensity line (blue).

In order to show the design conveniently, we simplify Eq. (S2) by some characteristic functions:

$$A(\rho) = (-1)^N \sin^2 \theta_N \frac{J_1(k\rho \sin \theta_N)}{k\rho \sin \theta_N}, \quad (\text{S4})$$

$$C(\theta_n) = 2 \cdot (-1)^n \sin^2 \theta_n, \quad (\text{S5})$$

$$S(\rho, \theta_n) = \frac{J_1(k\rho \sin \theta_n)}{k\rho \sin \theta_n}, \quad (\text{S6})$$

so that we have

$$U(\rho) = A(\rho) + \sum_{n=1}^{N-1} C(\theta_n) S(\rho, \theta_n), \quad (\text{S7})$$

without the constant item  $f^2$  in Eq. (S2). According to the above discussion, beyond the central position  $\rho=0$ , we still need to prescribe  $N-2$  zero-intensity positions in the region  $0 < \rho < D/2$ , which are shown from 2 to M in Fig. S3. The prescribed zero-intensity positions are labeled as  $m$  ( $m=1, 2, \dots, M$ ) to distinguish from the belt label  $n$ , resulting that the prescribed zero-intensity positions can be labeled as  $\rho_m$  ( $m=1, 2, \dots, M$ ). According to Eq. (S7), we have the M equations for M positions as follows:

$$\begin{aligned} A(\rho_1) + C(\theta_1)S(\rho_1, \theta_1) + C(\theta_2)S(\rho_1, \theta_2) + \dots + C(\theta_n)S(\rho_1, \theta_n) + \dots + C(\theta_{N-1})S(\rho_1, \theta_{N-1}) &= U(\rho_1) = 0 \\ A(\rho_2) + C(\theta_1)S(\rho_2, \theta_1) + C(\theta_2)S(\rho_2, \theta_2) + \dots + C(\theta_n)S(\rho_2, \theta_n) + \dots + C(\theta_{N-1})S(\rho_2, \theta_{N-1}) &= U(\rho_2) = 0 \\ &\vdots \\ A(\rho_m) + C(\theta_1)S(\rho_m, \theta_1) + C(\theta_2)S(\rho_m, \theta_2) + \dots + C(\theta_n)S(\rho_m, \theta_n) + \dots + C(\theta_{N-1})S(\rho_m, \theta_{N-1}) &= U(\rho_m) = 0 \\ &\vdots \\ A(\rho_M) + C(\theta_1)S(\rho_M, \theta_1) + C(\theta_2)S(\rho_M, \theta_2) + \dots + C(\theta_n)S(\rho_M, \theta_n) + \dots + C(\theta_{N-1})S(\rho_M, \theta_{N-1}) &= U(\rho_M) = 0 \end{aligned}$$

which can be simplified further by a matrix equation

$$\mathbf{S}\mathbf{C} = \mathbf{A}, \quad (\text{S8})$$

where  $\mathbf{S}$  is an  $M \times (N-1)$  matrix with its matrix element  $S_{mn} = S(\rho_m, \theta_n)$ ,  $\mathbf{C}$  is a  $(N-1) \times 1$  matrix with its matrix element  $C_n = C(\theta_n)$  and  $\mathbf{A}$  is an  $M \times 1$  matrix with its element  $A_n = -A(\rho_m)$ . Eq. (S8) is a non-linear matrix equation because the  $\mathbf{S}$  and  $\mathbf{C}$  are dependent on the unknown parameters  $\theta_n$ . In Eq. (S8), the number of unknown parameter and equations are the same so that it has the only solution. For a special position  $\boldsymbol{\rho} = [\rho_1, \rho_2, \dots, \rho_M]$ , which is up to the customized requirement in the size of D shown in Fig. S3, we just solve the non-linear equation shown by Eq. (S8) to finish the design of binary phase by fixing the angles  $\theta_n$  ( $n=1, 2, \dots, N-1$ ). Comparing with the solution of a linear matrix equation, the non-linear matrix equation in Eq. (S8) can not be solved by the simple matrix-inversion technique that is used to solve the linear matrix equation. In fact, for the non-linear matrix equation, it generally has no analytical solution but its numerical solution can be obtained in a quite easy way by using the well-developed Newton theory, which is widely used in the relative engineering problems [S3]. For the detailed process to solve Eq. (S8), we ignore it here because there are so many references about it. In addition, one can also find the

special packages to solve the non-linear matrix equation in some commercial computing software, e.g. MATLAB or MATHEMATICA. For the detailed information about our codes used to solve Eq. (8), one can refer to our new paper [S4]. Therefore, the solution of Eq. (S8) is not a troublesome issue. Sometimes, for one special position  $\rho$  (e.g.  $\rho_m$  and  $\rho_{m+1}$  are too close), the mathematical solution, provided by Newton's theory, of Eq. (S8) might be not a physical solution and we should drop it automatically. For a physical solution, it should satisfy the condition:  $0 < \sin\theta_n < \sin\theta_N$ .

In Fig. 5a, we show the four sets of designed binary-phase plates for generating the anti-resolution PSF using the problem in Eq. (S8). We choose the zero-intensity position at  $\rho=[0, 22.5\mu\text{m}, 45\mu\text{m}, 67.5\mu\text{m}, 90\mu\text{m}]$  for No. 1,  $\rho=[0, 27.5\mu\text{m}, 75\mu\text{m}, 82.5\mu\text{m}, 110\mu\text{m}]$  for No. 2,  $\rho=[0, 32.5\mu\text{m}, 65\mu\text{m}, 97.5\mu\text{m}, 130\mu\text{m}]$  for No. 3 and  $\rho=[0, 37.5\mu\text{m}, 75\mu\text{m}, 112.5\mu\text{m}, 150\mu\text{m}]$  for No. 4. The NA of focusing lens is fixed to 0.005 when we design the four sets of binary-phase plates. The data for the four sets of binary-phase plates are shown in Fig. 5a. For the design, we have to claim several points:

1) Both number of equations and unknown parameters in Eq. (S8) are the same (N-1) so that it has the only solution, but in real design by solving the Eq. (S8), the number of equations can be larger than (N-1) by prescribing more zero-intensity position in  $\rho$  (as shown in the above examples: four unknown parameters  $\theta_n$  ( $n=1, 2, 3$  and 4) but we prescribe five zero-intensity positions). The reason for this is to suppress the null field in the range of D. Another issue caused by this is that Eq. (S8) has no exact solution for the more zero-intensity position at  $\rho$ . But, this will not lead to the failure of designing the anti-resolution PSF because we only need the approximate solution numerically with the condition that the null-field ( $0 \leq \rho < D$ ) intensity is much below the sidelobe intensity. In our case, we take it as the null field when its intensity is below  $10^{-3}$  of the sidelobe intensity. Therefore, although we can not get the exact solution when we increase the number of the prescribed zero-intensity position, we can still get another solution to realize the anti-resolution PSF with more low intensity in the null-field region.

2) Because the binary-phase plate has the intrinsic property that can generate the null field at its Fraunhofer diffraction region, the focusing lens can not change the property and just transfer the Fraunhofer diffraction region to the focal region of focusing lens. Therefore, we design the four sets of binary-phase plates by using the

focusing lens with NA=0.005, but we show the axial size ( $d_0$ ) of the null field in the focusing lens with NA=0.0075 in order to match the experimental focusing lens in Fig. 4.

Finally, we have to emphasize that the method to design the binary phase plate for realizing the anti-resolution PSF is optimization-free because we can solve the inverse problem described in Eq. (S8) numerically by the well-developed Newton theory. It is worthy to point out that the optimization-free design method to control the optical field by a binary plate has been introduced to construct a super-oscillatory lens for realizing the super-resolution focusing.

## 5. Generation of optical capsule based on the anti-resolution PSF

In the last section, we have introduced the optimization-free design of binary phase for realizing the anti-resolution PSF. Now, we explain the physical reason for generation of optical capsule when the anti-resolution PSF is achieved at the focal plane.

First, we revisit the different focusing behavior along transverse and axial direction for a lens. Without loss of generality, we analyze the intensity at focal plane  $z=f$  for the transverse direction and the on-axis intensity with  $r=0$  for the axial direction. For the uniform illumination without any phase or amplitude modulation by binary elements, we can get the analytical form of the intensity at  $z=f$  and  $r=0$  according to Eq. (S1).

$$I(\rho, z=f) = \left| \int_0^R J_0\left(\frac{kr\rho}{f}\right) r dr \right|^2 = R^4 \left[ \frac{J_1(k\rho R/f)}{k\rho R/f} \right]^2, \quad (\text{S9})$$

$$I(\rho=0, z) = \left| \int_0^R e^{\frac{ikr^2}{2z}} e^{-\frac{ikr^2}{2f}} r dr \right|^2 = \frac{R^4}{4} \left\{ \frac{\sin \left[ R^2 k \left( \frac{1}{z} - \frac{1}{f} \right) \right]}{R^2 k \left( \frac{1}{z} - \frac{1}{f} \right)} \right\}^2, \quad (\text{S10})$$

where  $I(\rho, z=f)$  and  $I(\rho=0, z)$  show the intensity profiles at focal plane and on axis with  $\rho=0$ , respectively. From Eqs. (S9) and (S10), we can derive the size (from the focal point to the first zero-intensity) in radial and axial directions. For the radial size at the focal plane, the first zero-intensity point is located at  $k\rho R/f=3.84$ , which implies the radial size is

$$\Delta\rho = \frac{0.61\lambda}{NA}, \quad (\text{S11})$$

where  $NA \approx R/f$  for a low NA lens as shown by Fig. S4a- S4b. For the axial size with  $\rho=0$ , the first zero-intensity point is located at  $R^2k(1/z-1/f)=\pi$ , which implies that the axial size (Fig. S4a-S4c) is

$$\Delta z = \left| \frac{\lambda}{\lambda/f + 2(R/f)^2} \right| \approx \frac{0.5\lambda}{NA^2}, \quad (\text{S12})$$

From the radial and axial size denoted by Eqs. (S11) and (S12), one can see that the radial size is proportional to  $1/NA$  while the axis size is proportional to  $1/NA^2$ . Because the lens' NA is smaller than 1, the spot in radial direction is smaller than that in axial direction as shown in Fig. (S4), which indicates that the focusing lens has a tighter confinement in radial direction than axial direction. It is a very important as well as fundamental conclusion in optical focusing of lens. Therefore, for the well-built anti-resolution PSF at the focal plane, just standing on this physical conclusion without further investigation into the intensity distribution in axis region, we can have an intuitionistic prediction: the zero-intensity region in axis direction with  $\rho=0$  must be much larger than that in its radial region.

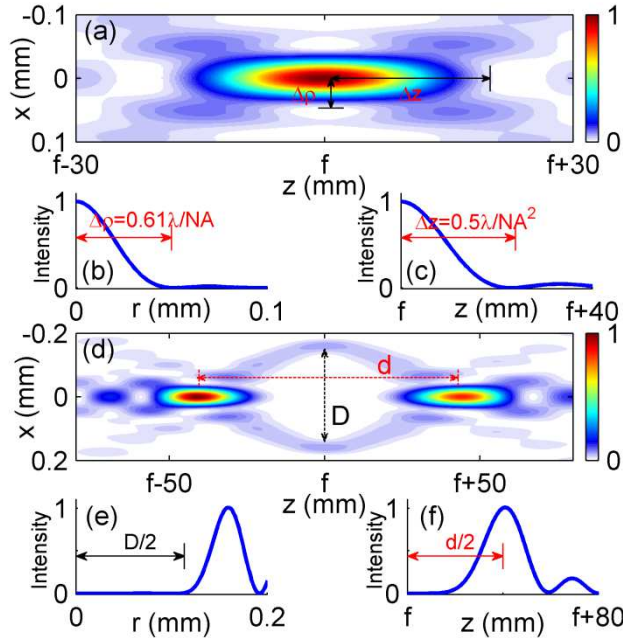


Fig. S4 The focusing properties of a lens. (a) The intensity profile at the x-z plane of focusing field by a lens. (b) The radial intensity profile of the focused spot at the focal plane in (a). (c) The axial intensity profile at  $\rho=0$  in (a). (d) The intensity profile of optical capsule in the focal region by using a lens and a binary-phase plate. D and d is the radial and axial sizes (from one hotspot to another) of the optical capsule. (e) The

radial intensity profile of the optical capsule at the focal plane in (d). (f) The axial intensity profile of the optical capsule at  $\rho=0$  in (d).

Next, we check the above prediction through the analytical simulation by using Eq. (S1) because this theoretical prediction proves the generation of optical capsule on the basis of anti-resolution PSF. In fact, the simulation results in Fig. 5c-5c have proved the prediction that the transversal ( $D$ ) and axial sizes ( $d_0$ ) are proportional to  $1/NA$  and  $1/NA^2$ , respectively. Because  $NA < 1$ , the axial size ( $d_0$ ) is always larger than the transversal size ( $D$ ). Although we can find the undoubtable proof to verify the existence of the axial null-field from the simulation in Fig. 5c, we can also find another physical proof based on the uniform variation of energy flux of light in the homogenous medium. In section 4, we showed the generation of the anti-resolution PSF with the null-field region  $0 \leq \rho < D$  at the focal plane. If we move the viewing position to one out-of-plane ( $z \neq f$ ) position, we can predict the existence of null field at this out-of-plane position because of the uniform variation of energy flux of light in air as shown in Fig. S4d. The null-field region will exist until the out-of-plane position is located at the two ends of the optical capsule. Because the axial confinement of focusing lens is much weaker than its transversal confinement, as shown by Eqs. S11 and S12, the null field in axial direction has the longer extension than that in transversal direction. Therefore, an optical capsule with long boundary in axial direction and short boundary in transversal direction is formed after an anti-resolution PSF has been generated at the focal plane.

The sections 4 and 5 are contributed to explain the physical reason for the generation of optical capsule by using the novel anti-resolution PSF concept in the optical imaging system with focusing lens, which motivates us to propose the optical capsule in theory and verify it in experiment. However, the basic reason is the substantial property of the binary-phase plate in generating the optical capsule at its Fraunhofer-diffraction region as depicted in the main text.

## References

- [S1]. K. S. Youngworth, T. G. Brown, *Opt. Express* **7**, 77 (2000).
- [S2] Min Gu, *Advanced optical imaging theory*, **75** (Springer-Verlag, New York, 1999)
- [S3] J.E. Dennis, R.B. Schnabel, *Numerical methods for unconstrained optimization*

and nonlinear equations, New Jersey: Prentice-Hall, 1983.

[S4] K. Huang, P. Ye, J. H. Teng, et.al. “Optimization-free super-oscillatory lens using amplitude and phase masks”, *Laser Photonics Review*, **8**, 152 (2014).